Nonlinear dynamics in a backward-facing step flow

H. P. Rani and Tony W. H. Sheu[a)]
Department of Engineering Science and Ocean Engineering, National Taiwan University, Taipei, 106 Taiwan, Republic of China

(Received 29 December 2005; accepted 29 June 2006; published online 17 August 2006)

A numerical investigation has been conducted to explore the complex nonlinear nature of flow in a backward-facing step channel by the simulated results, which include the bifurcation diagram, limit cycle oscillations, power spectrums, and phase portraits. For small values of Reynolds number, the flow was steady and laminar. When the Reynolds number was amplified, the flow becomes unsteady with the initiation of a supercritical Hopf bifurcation. The flow path is trapped by the stable limit cycles, and this system is made to proceed with a sustained oscillation. As the Reynolds number was amplified further, the stability of the investigated system keeps decreasing through a sequence of frequency-doubling bifurcations. The fundamental frequency of high amplitude was identical to the most amplified mode of Kelvin-Helmholtz instability oscillations in the shear layer. Frequencies with a small amplitude result in a slower development of the Kelvin-Helmholtz instability and are responsible for the roll-up of the shear layer. The phase portrait shows the evolution of a chaotic attractor from a simple periodic attractor. Prior to the onset of the chaotic motion, pitchfork bifurcation showed its existence. © *2006 American Institute of Physics*. [DOI: 10.1063/1.2261852]

I. INTRODUCTION

Nonlinear phenomena in pragmatic systems are often observed in the experimental work. This is followed by conducting the simulation study and the subsequent detailed analysis to provide explanations for the observed experimental phenomena. One such investigation is the channel flow with reversals. Moreover, if the analytical/numerical results are unearthed, experiments are indispensable for verifying these simulated results. One such experimental work of Nie and Armaly,[1] who extensively studied the flow in a backward-facing step channel, provided a path to validate the present simulated results. Though the flow over a backward-facing step is simple in geometry, it nonetheless can exhibit complex flow separation and reattachment. The flow in this backward-facing step channel can be regarded as an entry flow within the two parallel vertical endwalls, a roof and a floor, followed by a confined recirculating flow behind a step wall [as shown in Fig. 1(a)]. This expansion flow has attracted a great deal of attention over the last few decades.[2–5] Also, this problem is a noteworthy example for the separated flow that occurs in aerodynamic devices such as high-lift aerofoils at high angles of attack. Flow separation may be created by a strong adverse pressure gradient rather than by a geometric perturbation. From the fundamental perspective, the instability and the transition to turbulence in this open channel flow are of great importance. Transition mechanisms in parallel flows such as plane channels and pipes have received substantial attention.[6–8] This basic flow in the plane channel can be more well understood than some of the nonparallel flows arising in more complex geometries.

In this context the flow over a backward-facing step has emerged as a prototype of a nontrivial yet simple geometry and is, thus, proper to examine the onset of turbulence.[9–13] From a computational perspective, the steady two-dimensional flow over a backward-facing step is an established benchmark problem.[14,15] The two-dimensional, absolute, linear stability of this flow has been examined extensively and was discussed in several publications.[15–17] Computational studies have enlightened that this two-dimensional laminar flow is linearly stable with respect to the two-dimensional perturbations until a Reynolds number (Re) of at least 600. Experiments by Armaly and others[4] for the airflow in a backward-facing step geometry with a nominal expansion ratio of approximately two provided a quantitative measurement of two- and three-dimensional flows over a large range of Re from 50 to 6000. Besides providing the data on separation and reattachment points, the streamwise velocity measurements are reported for several Re throughout their study. They also showed that below Re=300 the flow is essentially spanwise invariant, although a visible deviation from the two-dimensionality exists near the lateral sidewalls of the channel.

Williams and Baker[18] have conducted the three-dimensional (3-D) simulations in a domain with lateral sidewalls having the same expansion and aspect ratios (spanwise length to step height) used by Armaly and others,[4] who reproduced the experimental laminar 3-D flow. They noted that the transition from two- to three-dimensional flow is not an abrupt change but is rather a continuous penetration of the 3-D flow, fed by a wall jet, from the sidewall to the central symmetry plane. They observed that the three-dimensionality of the flow does not follow from a fundamental hydrodynamic instability of the two-dimensional flow. More recently, Nie and Armaly[1] presented the 3-D experimental results for Re in the range between 100 and 8000, thus covering the laminar, transitional, and turbulent flow regimes. They showed that for increasing Re the size of the reverse flow

[a)]Author to whom correspondence should be addressed. Electronic mail: twhsheu@ntu.edu.tw

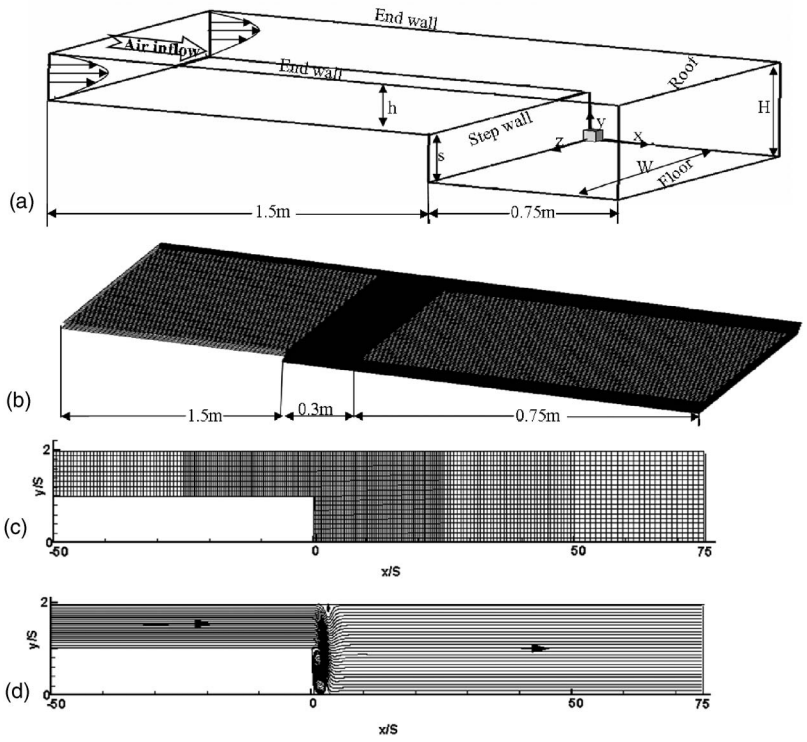

FIG. 1. (a) Schematic of the backward-facing step flow problem under the current investigation; (b) schematic of the generated 3-D mesh; (c) projection of the generated mesh on the xy plane at $z/S=4$; (d) streamlines for Re=2000 at $z/S=4$.

region increases and moves farther downstream in the laminar flow regime; decreases and moves upstream in the transitional flow regime; and remains almost unchanged or diminishes in the turbulent flow regime. Armaly and others[19] in their experimental measurements revealed that a swirling jet-like flow develops near the sidewall in the separated shear layer, which could not be deduced in the two-dimensional studies.

In the nonlinear flow system, many bifurcation types leading to chaotic flow from simple laminar flow can be observed. Typical examples are the pitchfork (symmetry-breaking), transcritical, saddle-node, Hopf, flip (or tangent), Niemark (or secondary Hopf), homoclinic, period-doubling, frequency-doubling, and catastrophic bifurcations. Bifurcation can be defined as a qualitative change of the flow behavior in a nonlinear system. In the bifurcation theory, these bifurcations can be classified as static and dynamic. In the static bifurcations the most common and important bifurcations are the saddle-node, transcritical, and pitchfork bifurcations. The Hopf, period-doubling, and frequency-doubling bifurcations are the common dynamic bifurcations. Furthermore, the bifurcations can also be classified as local and global types based on their equilibrium points. Local bifurcation involves one or more equilibrium solution points while the global bifurcation involves the appearance or disappearance of the equilibrium points. Our attention was paid exclusively to the Hopf, frequency-doubling and pitchfork bifurcations because of their existence in the currently investigated channel flow.

The bifurcation types illustrating the transition to chaos are most commonly characterized by their power spectrums and phase portraits. Hakin[20] used the Lyapunov exponents and Grassberger and Procaccia[21] used the correlation dimension to distinguish various attractors quantitatively. To describe the flow bifurcation, the legitimate bifurcation analysis that goes beyond the linear stability analysis was conducted. The nature of bifurcations, which arise as a result of the developing disturbances, is deliberated based on the limit cycle oscillation theory.[22] The bifurcation types involved in the present system were studied based on the L_2 error norms, time-evolving solutions, power spectrums, and phase portraits.

Due to the occurrence of periodic oscillations in the present channel flow, the flow stability in the backward facing step channel is analyzed. The stability study of the nonlinear system is significant to determine whether this system can exhibit self-sustained oscillations, i.e., whether the invoked system will oscillate even in the absence of an external driving force (e.g., rhythms in the body temperature, heartbeat, hormone secretion, and chemical reactions that oscillate spontaneously). Also, from the stability analysis it can be known whether the system can return to the stable limit cycle if it is perturbed.

In spite of the several investigations of channel flow over a backward-facing step that are available in the literature, we wish to address the following: the critical Re at which the flow becomes unstable and the nature of bifurcation leading to chaos. This is similar in spirit to the experimental work of Nie and Armaly[1] to quantify the transition to three-dimensionality and, finally, to turbulence via the backward-facing step simulations. Based on their work, an attempt was made to examine 3-D convective instability of the backward-facing step. This work was further extended to nonlinear stability computations to determine whether the bifurcations are supercritical or subcritical. The computational results presented in this paper will expand the database for this nonlinear benchmark problem in three dimensions.

The rest of the paper is organized as follows. In Sec. II

we introduce the formulation of problem along with the physical parameters. In Sec. III we address the computational methods and the validation of the code that is used to carry out the current simulation. In Sec. IV the results will be analyzed based on the flow nature, vortex stability, and bifurcation theory for a wide range of Re. The bifurcation types are identified based on the limit cycles, time-series, power spectrums, phase portraits, and L_2 error norms. Finally, in Sec. V, a summary of the present study is provided.

II. COMPUTATIONAL DOMAIN

In Fig. 1(a), the 3-D schematic diagram of the investigated backward facing step problem is shown. In this study, the step geometry and the flow conditions considered by Nie and Armaly[1] were chosen to enable the direct comparisons with the experimental results. The step height (S) and the duct width (W) are assumed as 0.01 and 0.08 m, respectively. The upstream (h) and downstream ($H=h+S$) duct heights of the expansion are assumed to be 0.0098 and 0.0198 m, respectively. This geometry provides a configuration with an expansion ratio [ER$=H/(H-S)$] of 2.02 and an aspect ratio (AR$=W/S$) of 8. The origin of the coordinate system is located at the intersection of the bottom corner of the step wall and vertical end wall, as shown in Fig. 1(a). The directions of the streamwise (x), transverse (y), and spanwise (z) coordinates are also shown in the figure. The streamwise length of the computational domain is 1.5 m in upstream and 0.75 m downstream from the step wall, i.e., $-150 \le x/S \le 75$. This choice was made to ensure that the flow at the inlet section of the duct ($x/S=-150$) is not affected by the sudden expansion in geometry. To justify the existence of fully developed flow present at the exit plane, in Fig. 1(d) the streamlines at $z/S=4$ for Re$=2000$ are shown. It is observed that the flow at the exit section of the duct ($x/S=75$) can be treated as fully developed. It was confirmed that the use of a longer computational domain did not change the flow in the region downstream from the step and discussed in Sec. III B. In the present problem the physical properties of air are treated as constants and are assumed as density (ρ)$=1.205$ kg/m^3, and dynamic viscosity (μ)$=1.81\times10^{-5}$ kg m^{-1} s^{-1}. Inlet flow ($x/S=-150$, $1 \le y/S \le 1.98$ for all z) was considered to be hydrodynamically steady and fully developed with the streamwise velocity component (u). The other velocity components (v and w) were set as zero at the inlet section. The no-slip boundary condition (zero velocity vector) was applied at all the wall surfaces. Fully developed velocity conditions were imposed at the exit section ($x/S=75$, for all y and z) of the physical domain.

III. BASIC EQUATIONS AND METHOD OF SOLUTION

A. Basic equations

A study of the unsteady nature of a flow through the currently investigated 3-D backward-facing step channel requires the solution of the following nonlinear set of coupled partial differential equations, which express the mass and momentum conservations:

$$\nabla \cdot \bar{V} = 0, \tag{1}$$

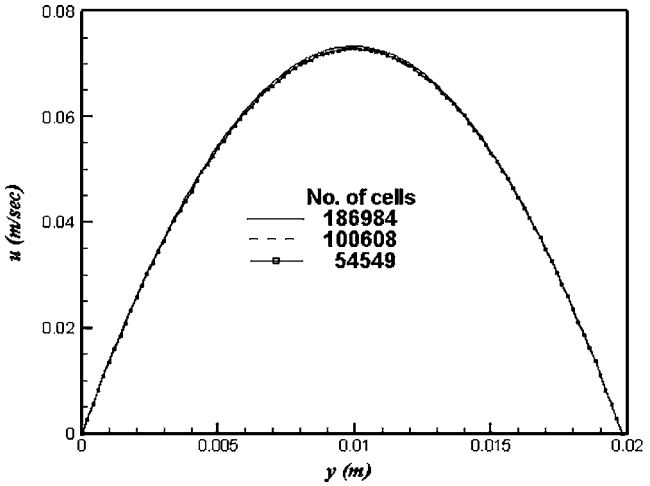

FIG. 2. Grid independent validation test for the case considered at Re$=100$. The streamwise velocity solutions are plotted at the symmetry plane and $x/S=10$.

$$\frac{\partial \bar{V}}{\partial t} + (\bar{V} \cdot \nabla)\bar{V} = -\nabla P + \frac{1}{\mathrm{Re}}\nabla^2 \bar{V}. \tag{2}$$

In the above elliptic-parabolic mixed-type differential equations, $\bar{V}=(u,v,w)$, P, and t represent the velocity vector, pressure, and time, respectively. In the following sections, the three velocity components u, v, and w are referred to as the streamwise, transverse, and spanwise velocities, respectively. The Re is given by $\rho u_0 D_h/\mu$, where D_h is given as $2Wh/(W+h)$ and u_0 denotes the average initial velocity. Note that this definition for Re is the same as the one used by Nie and Armaly.[1]

B. Computational details

The numerical simulation of the governing equations (1) and (2) subjected to the boundary conditions described above was performed by utilizing the commercial computational fluid dynamics software CFDRC. The mesh is generated from the structured block volume elements using the preprocessor CFD-GEOM. The nonuniform grid distribution with $\Delta x_{\min}=0.15$ cm; $\Delta y_{\min}=0.039\,26$ cm; $\Delta z_{\min}=0.2$ cm [shown in Figs. 1(b) and 1(c)] was selected to ensure high density near the bounding walls and in the regions near the step, where the high gradient solution profiles exist, so as to ensure the accuracy of the simulations. The 3-D continuity and Navier-Stokes equations (1) and (2) for the investigated incompressible fluid flow were solved numerically using the finite volume method. The AMG (Algebraic Multi Grid) algorithm was used for the pressure-velocity coupling and the momentum equations are discretized with the third-order upwind scheme in order to pursue higher accuracy of the simulations. The SIMPLEC scheme has been adopted for the pressure correction. For the unsteady calculations, the first-order accurate unconditionally stable implicit backward Euler time stepping method was used. A typical time increment was set as 0.001 s. At the end of each iteration, the residual sum for each of the conserved variables was computed and stored to record the convergence history. The convergence

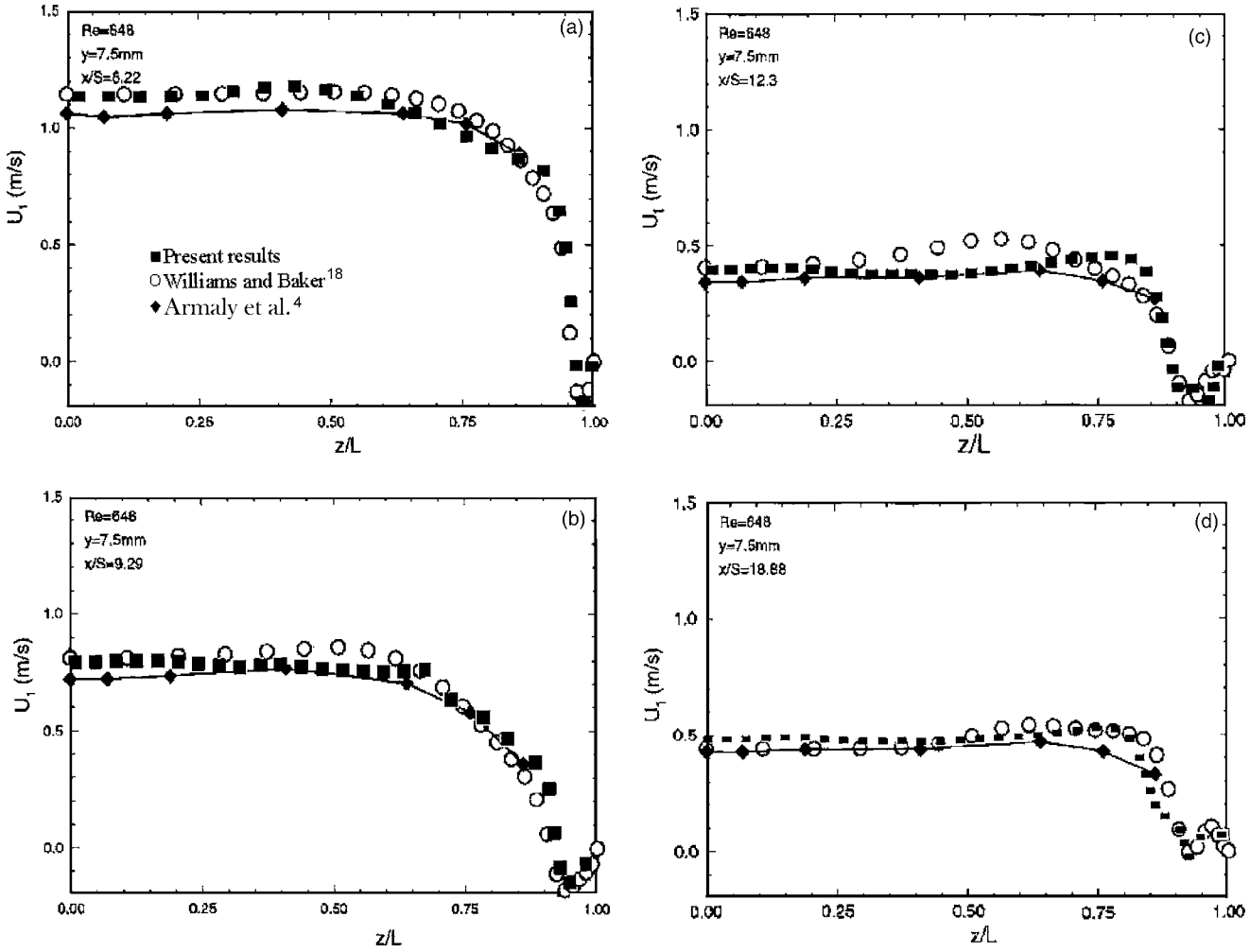

FIG. 3. A comparison of the present, numerical, and experimental spanwise velocity profiles for Re=648 at $y=7.5$ mm and (a) $x/S=6.22$; (b) $x/S=9.29$; (c) $x/S=12.3$; (d) $x/S=18.88$.

criterion requires that the scaled residuals must be smaller than 10^{-10} for the mass and the momentum equations. The convergence of a solution was also checked from both mass flow summaries. For example, at Re=740, the flow imbalance ($2.092\,51\times10^{-17}$) was 13 orders of magnitude smaller than the inflow or outflow ($\sim\pm5.834\,31\times10^{-4}$). Hence this is a well converged solution in the sense that an imbalance in three to four orders of magnitude smaller than the inflow/outflow typically indicates good convergence.

The mass flux was calculated to find out whether there was any inflow through the outlet ($x/S=75$). As the exit section of the channel was drawn far enough from the step wall, the mass flux was observed to be zero. When the downstream length was $x/S<75$, the flow disturbances near the outlet lead the fluid to come back into the system. This implies that the fully developed flow was not obtained and gives rise to convergence problems. Hence in the present study the downstream length was chosen as $x/S=75$. Detailed descriptions of the CFD code and the solution procedures can be found in the CFDRC manual. The simulated results were viewed and analyzed in the 3-D animated plotting tools like the CFD-VIEW and the TecPlot.

Three stages of mesh refinement shown in Fig. 2 were investigated starting with 54 549 nodes, then with 100 608 nodes, and progressing to the final mesh of 186 984 nodes for Re=100. From Fig. 2, it is observed that the streamwise velocity did not show much variation when the 100 608 nodes were increased by 50%. Hence, the grid with 100 608 nodes was used for calculating all the results that are presented in this paper. A detailed study of the grid dependence of the present results had not been performed with still finer grids, because it would require a prohibitively large computer capacity.

C. Code validation

The simulated spanwise velocity profiles were compared with the numerical and experimental results of Williams and Baker[18] and Armaly *et al.*[4] at $y=7.5$ mm for Re=648 and are shown in Fig. 3. Armaly *et al.*[4] reported that at this Re the flow is fully three dimensional, as confirmed by the variation in the axial velocity across the lateral span of the flow field. In general, very good agreement is observed between the present simulation and the numerical and experimental data at all x stations. The persistent flow reversals near the sidewall, missed in the experiments owing to their limited range,

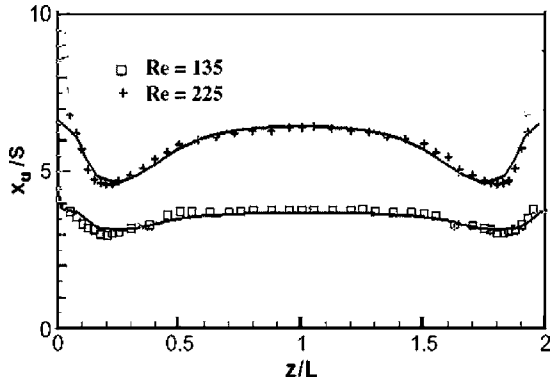

FIG. 4. A comparison of the x_u lines (skin-friction lines) on $y/S=0.05$ plane between the present simulation (solid lines) and the experimental results of Nie and Armaly (Ref. 1).

are an indication of significant flow separation and, hence, reversal along the duct sidewall for $x/S \leq 18$.

Further, an attempt was made to compare the simulated laminar results with the available experimental results of Nie and Armaly[1] and the resulting comparison is found to be satisfactory, as shown in Fig. 4. The results in the transitional and turbulent regions, presented by the same authors, are hard to compare, since there exist no details about the time at which the transient results are shown.

IV. RESULTS AND DISCUSSION

The flow structure depends on the geometrical parameters (H, h, S, and W) and the control parameter Re. In the present work, the effect of Re was studied by keeping the other geometrical parameters fixed. The computations were started at Re=100. At this low Reynolds number the simulated flow field was observed to be steady and laminar. Figure 5 shows the steady state solutions obtained at different Re. With the increasing values of Re, the flow in the present dynamical system was observed to transit from one equilibrium state to another due to the presence of a rapidly varying disturbance field. It was found that the flow remained steady

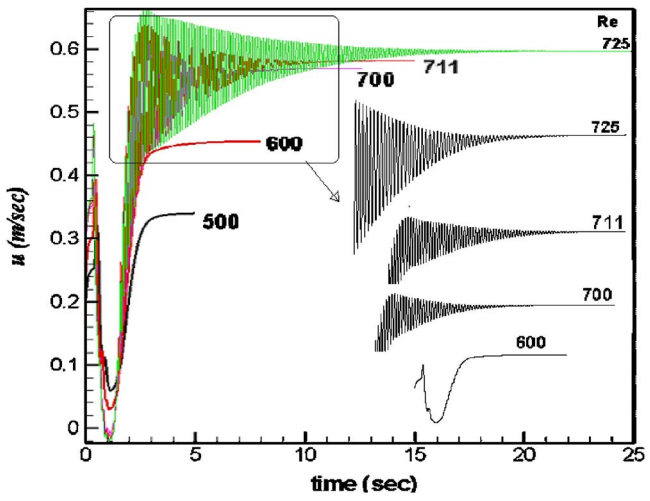

FIG. 5. (Color online) The simulated time-evolving streamwise velocity for various Re.

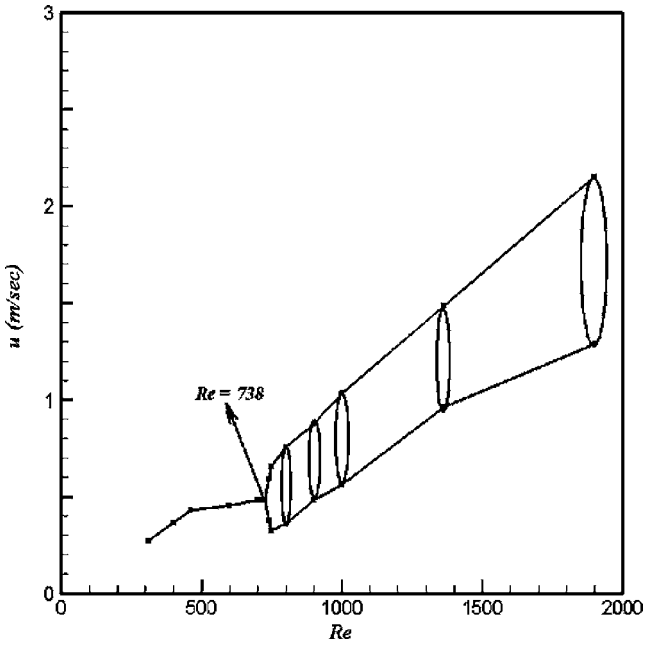

FIG. 6. The bifurcation diagram based on the simulated streamwise velocity at the arbitrarily chosen location (10, 1, 4).

until Re=735. At the slightly increasing Reynolds number Re=738, the flow, however, starts to exhibit a time-periodic solution. Since the unsteady equations were taken into consideration, the computational results signify that for Re<738 the flow became time asymptotically steady, whereas at Re=738 it evolved to exhibit a limit cycle (or periodic attractor). The bifurcation diagram in Fig. 6 shows the existence of two solutions for the streamwise velocity component as Re≥738. First, the flow topology was presented to show a global skeleton of the flow development in the investigated backward step for Re=1000. Then, the nonlinear theory was studied based on the vortex stability and bifurcation. The transitional flow leading to the chaotic flow is analyzed with the aid of limit cycles, time-series, phase portraits, power spectrums and L_2 error norms for wide range of Reynolds numbers.

A. Nature of the flow

To extract the meaningful flow physics from the 3-D unsteady flow structure, the topology of the limiting streamlines (the streamlines passing very close to the solid wall) or skin friction lines were depicted. Figure 7 illustrates the global picture of the 3-D flow development in the backward-facing step for the transitional flow region (Re=1000). It is seen from this figure the wavy streamlines along the symmetry plane and the limiting streamlines adjacent to the step wall, channel roof, floor, and vertical endwall at the instant of maximum velocity in the downstream. This illustration would help us to visualize the global structure of the vortical flow. On the floor plane, the attachment and separation lines are shown. These topologically singular lines appeared to be the barriers in the flow field. The region within the lines of separation and reattachment is hereinafter referred to as the recirculation region, which is our main interest in the present

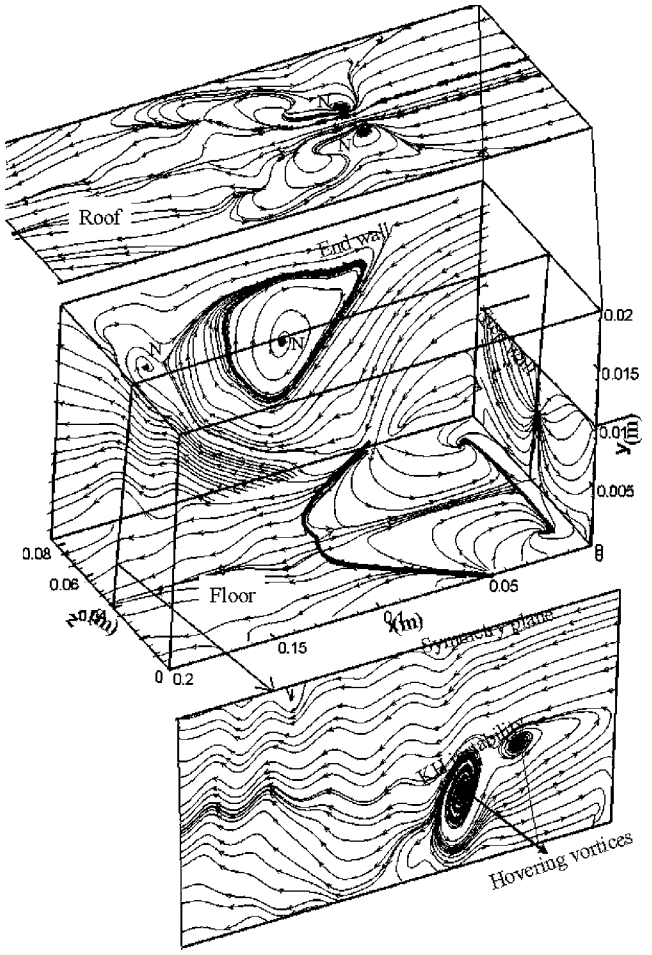

FIG. 7. The simulated streamlines near the endwall at $z/S=0.05$, symmetry plane at $z/S=4$, floor plane at $y/S=0.05$, roof plane at $y/S=1.93$, and the step wall at $x/S=0.05$ for $\mathrm{Re}=1000$ at $t=4.04$ s. The dark lines on the floor plane denote the attachment/separation lines and N denotes the spiraling nodes.

study. The flow physics in this recirculation zone will be discussed in detail in the following sections. Two spiral nodes are seen at all the planes. The nodes present below the separated shear layer are referred to as the periodically produced hovering vortices. Such hovering vortices play a critical role in the formation of Kelvin-Helmholtz (KH) instability, which will be discussed also later in detail. Beyond the reattachment region, no vortex appears to exist, and the only trace of the periodicity was the undulation of the streamlines. The flow in the rear end of the step plane is found to be divided into two regions from the symmetry plane, with one region rotating in the clockwise direction while the other in the counterclockwise.

To get a clear picture of the deformations about the recirculation region, the streamwise velocity is plotted against time and is shown in Fig. 8(i). It is observed that the flow velocity oscillates periodically. The recirculation region undergoes severe deformation during each time interval. To illustrate the deformations, the flow was observed at four instances that were marked as (a)–(d) in Fig. 8(i). The recirculation regions at these four time intervals are highlighted in Figs. 8(ii), (iii), (iv), and (v) by means of the zero contours of streamwise velocity. In the present study, attention is paid only to the recirculation region near the step wall on the floor plane, due to its deforming nature, although there are another two nondeformed recirculation regions present near the roof plane in the downstream channel. Initially, when the velocity is maximum, i.e., at $t=4.04$ s, there exists a single recirculation region near the step wall, as shown in Fig. 8(ii). Once the velocity starts to decrease, i.e., at $t=4.05$ s, this region is split into two regions, I and II (large and small regions, respectively), as shown in Fig. 8(iii). Afterward, the region "II" bursts into small regions, i.e., at $t=4.07$ s [Fig. 8(iv)]. When the velocity reaches its minimum, i.e., at $t=4.08$ s the region "II" disappears, as shown in Fig. 8(v). Thus, for the decreasing velocity, the large recirculation region I will be split into small recirculation region II and this region II finally disappears in the subsequent time intervals, while for the increasing velocity the above processes are reversed. By virtue of the information about the deformation of the separation bubbles (recirculation region) provided in Fig. 8, it is possible to determine the time interval Δt between the appearance and disappearance of the new separation bubble and the time at which the recirculating flow reaches its maximum. In the present case the maximum time interval was observed to be 0.04 s. For every 0.08 s, the maximum reverse flow is reached or the two bubbles are attached to each other.

The maximum streamwise extent of the recirculation region is observed to depend on the time and Re, which in turn determine the duration of the deceleration period and the strength of the deceleration, respectively. As a consequence, at $\mathrm{Re}=1000$ a faster growth of the periodic recirculation "revival" of Region II was observed. Also, the apparently triggered KH instability for $\mathrm{Re}=1000$ leads to a faster roll-up of the shear layer, illustrated by the fact that the maximum reverse flow was reached at an earlier phase to promote the subsequent damage of the large separation region (I) as it was convected downstream.

B. Nonlinear dynamics

1. Vortex stability and limit cycle oscillations (LCO): Supercritical Hopf bifurcation

In the stability analysis it is important to grasp the property of the limit cycle (i.e., stable or unstable) when the system condition is near the Hopf bifurcation. In particular, the unstable limit cycle affects the global stability. In the subsequent discussions emphasis is given to the numerically predicted limit cycles around the vortex core at $\mathrm{Re}=1000$. The stability boundary formed by the limit cycle was assessed as a function of the velocity component tangent to the vortex core.

The vortex core shown in Fig. 9 was computed based on the velocity gradient eigenmode method. The hairpin-like vortex core line[23] has its origin/termination on the bounding floor plane. Figure 9(a) clearly shows the spiraling nature of the stream traces around the vortex core. It is observed that the system trajectory forms an orbit in the direction of the vortex core. This implies that the kinetic energy along the flow is wrapped around the vortex core. The spiraling stream

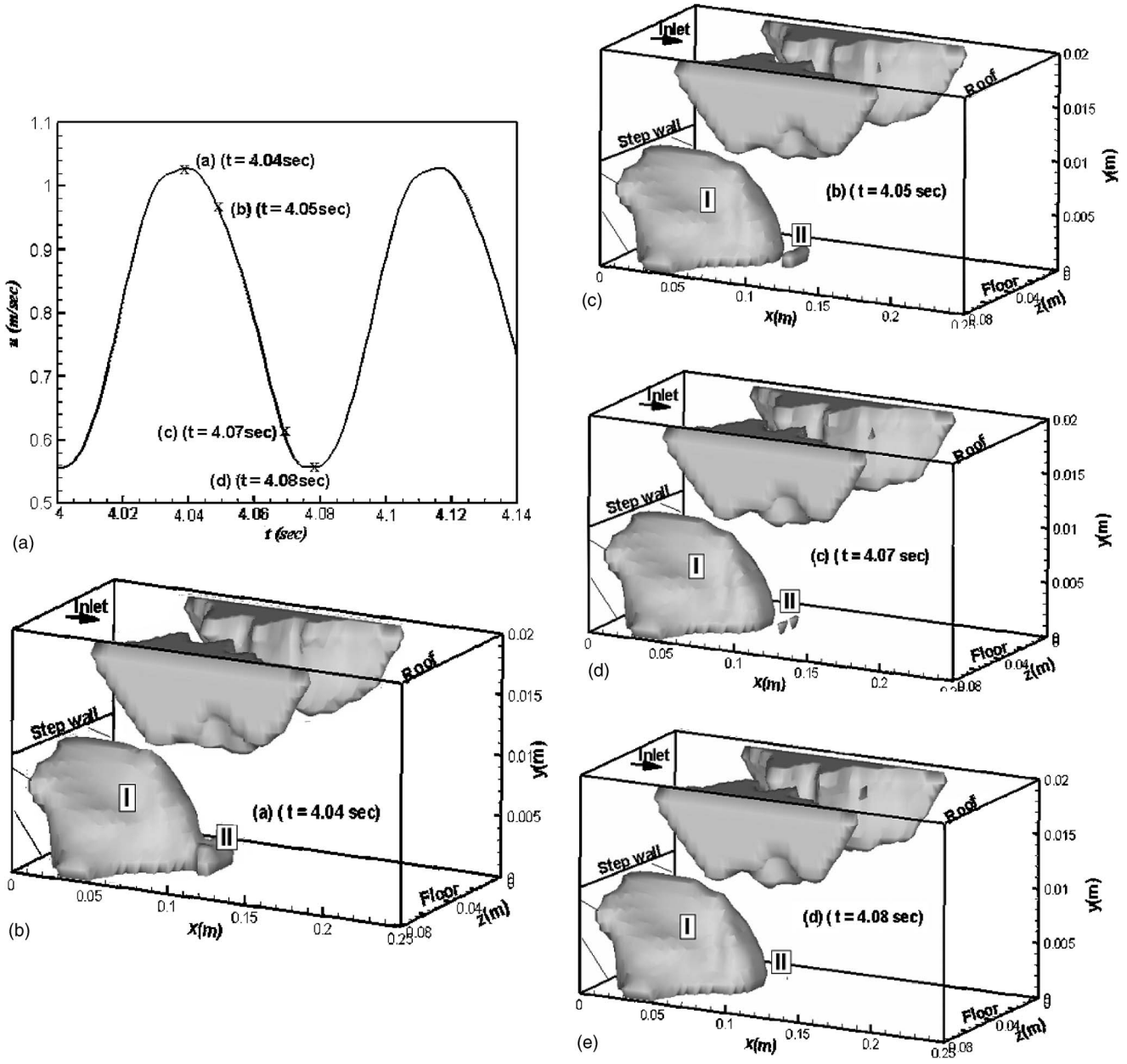

FIG. 8. The simulated time series and the zero contour plots for the streamwise velocity to illustrate the deformation of the recirculation regions (shaded regions), where I and II denote the two recirculation regions for Re=1000. (i) Time versus velocity component u; (ii) merging of regions I and II; (iii) breaking of regions I and II; (vi) breaking of region II; (v) disappearance of region II.

traces showed the distinguished nature at the three locations marked as L1, L2, and L3 in Fig. 9(a). At these locations the flow changed its direction and it is subjected to three alternate stable and unstable processes, where the Hopf bifurcation had its origin. These stable and unstable processes induced the limit cycle oscillations (LCO). At these three locations the limit cycles were drawn along with the vortex core and are shown in Fig. 9(b). It is observed that the sizes of limit cycles L2 and L3, which are of the same size, are smaller in comparison with that of L1. The stability of these limit cycles and the existence of a supercritical Hopf bifurcation are analyzed in the subsequent paragraphs.

To obtain a profound understanding of the vortex stability and LCO, the velocity gradient (λ) shown in Fig. 9(c) was calculated along the vortex core line. From Fig. 9(c) it is observed that λ changes its sign from positive to negative at three locations. These locations are of primary importance. The positive λ values show the flow acceleration along the vortex core and the negative λ values indicate the flow deceleration along with the vortex breakdown. Also, the zero λ values hint the limit cycle formation at those locations. Further, if λ has n number of sign changes then there exists n number of limiting cycles. There are three limit cycles found in the present nonlinear flow system and they are marked as L1, L2, and L3, as shown in Fig. 9(b). It is seen from the simulated limit cycles that they will separate the vortex into the inner unstable region (moving away from the vortex core) and the outer stable region (moving towards the vortex core). This implies that the stable limit cycles exist in the

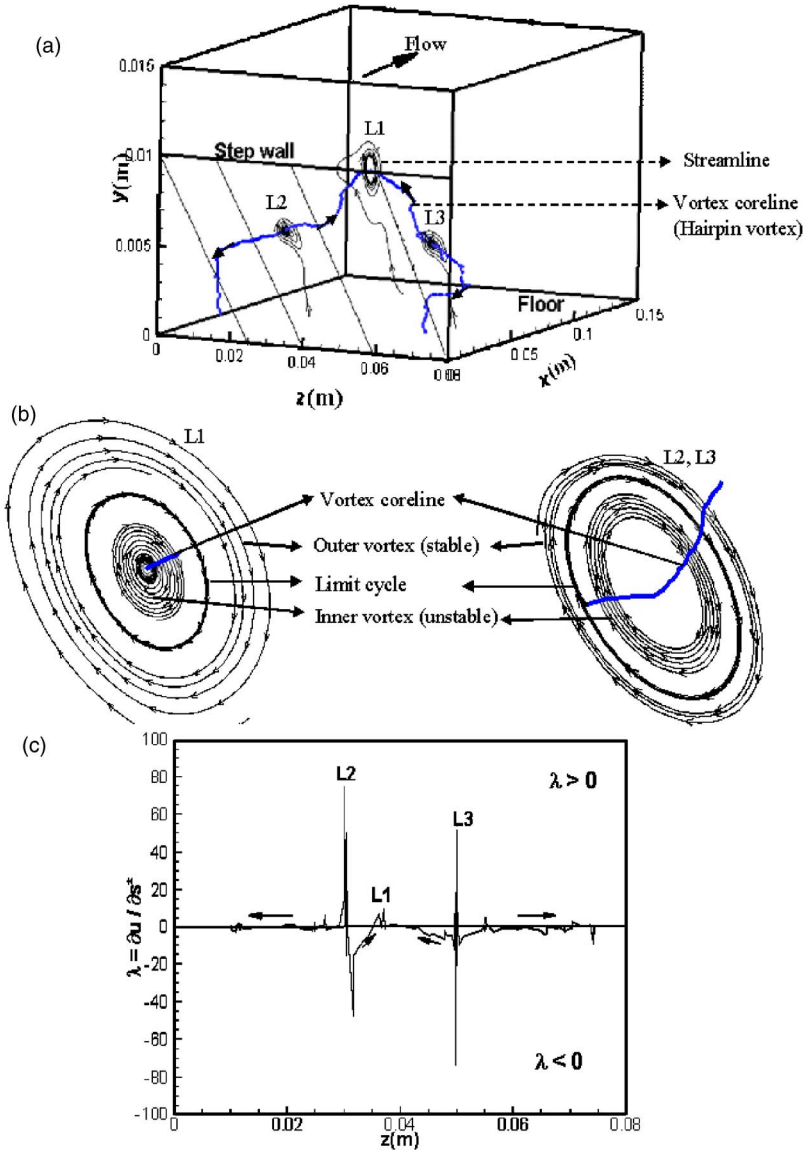

FIG. 9. Illustration of the supercritical Hopf bifurcation for Re=1000 at $t=8$ s. The arrows indicate the flow direction. L1, L2, and L3 denote the limit cycles. (a) Stream traces around the vortex core line; (b) stability of the limit cycles; (c) streamwise velocity gradient along the vortical core line (s^*).

current nonlinear system. From these stable limit cycles, the existence of supercritical Hopf bifurcation is now acknowledged.

The Hopf bifurcation is characterized by the appearance of a periodic orbit (or a limit cycle or an attractor), which can be classified as supercritical and subcritical. The frequently discovered supercritical Hopf bifurcation in the Navier-Stokes system involves a stability change from the critical point or a globally asymptotic stable equilibrium to the periodic orbit or a limit cycle. By virtue of the observed limit cycle the existence of supercritical Hopf bifurcation is explained as follows: From Fig. 9(a) it is seen that the larger limit cycle lies in between the two smaller limit cycles. Its presence is due to the fact that the stable equilibrium point oscillates and develops into a stable limit cycle. The limit cycle either grows until its magnitude becomes large enough (i.e., L2 or L3 → L1) or diminishes as the flow returns to the steady state (i.e., L1 → L2 or L3). Moreover, a branch of stable periodic solutions [the outer region in Fig. 9(b)] overlaps the branch of unstable solutions [the inner region in Fig. 9(b)]. This class of Hopf bifurcation is, therefore, regarded as the combination of the unstable focus and the stable limit cycle. It is implied that the stable limit cycle exists around the unstable inner region and forms a global stability boundary. The currently investigated 3-D backward-facing step channel flow is, therefore, known to have a supercritical Hopf bifurcation. As the flow path in the current nonlinear system was trapped by the stable limit cycles, the system is made to proceed with a sustained oscillation and does not lose the synchronization when it is perturbed. On the contrary, in the subcritical Hopf bifurcation, which is not observed in the current nonlinear flow system, a branch of unstable periodic solution overlaps the branch of stable solutions. Hence this bifurcation can be regarded as the combination of stable focus and unstable limit cycle.

2. Frequency-doubling bifurcation

The frequency-doubling bifurcation in the recirculation region is analyzed in terms of the time-series, phase portrait, and power spectrum of the simulated velocity components in the symmetry plane near the step wall at the point (10, 1, 4).

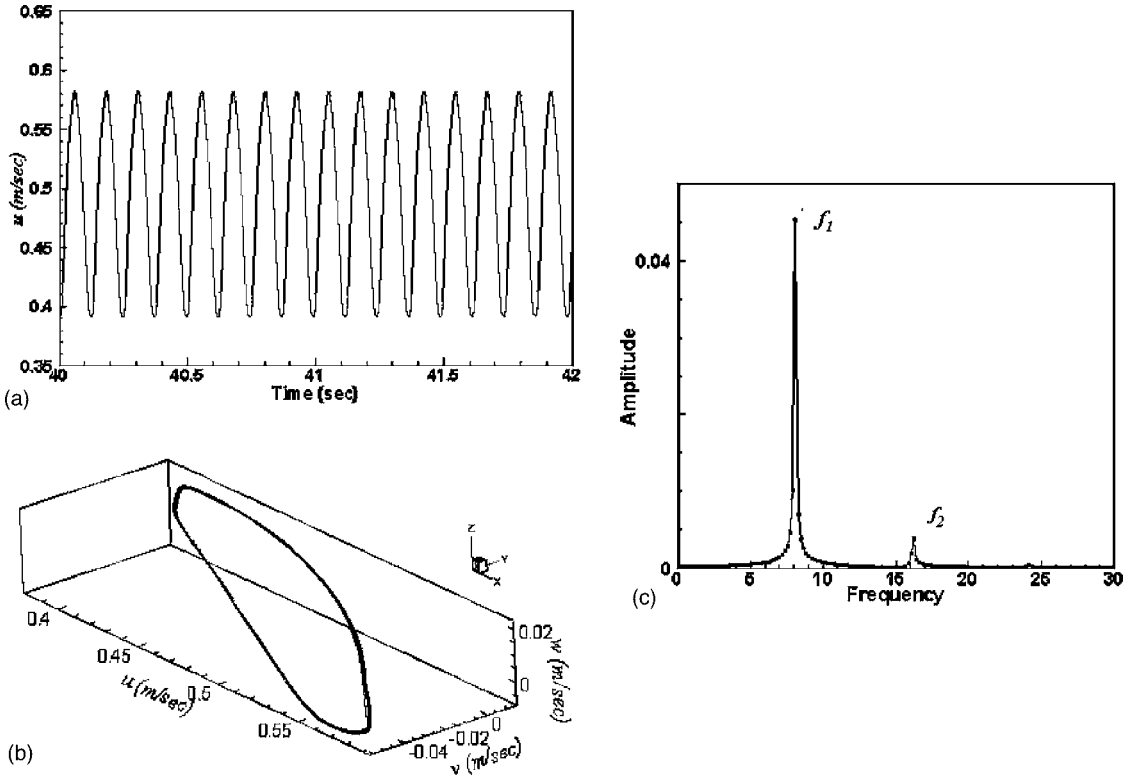

FIG. 10. The simulated (a) time series; (b) phase portrait; (c) power spectrum for Re=740 based on the solutions obtained at the point (10, 1, 4). f_1(=9) and f_2(=$2f_1$=18) denote the fundamental frequency and the arithmetically related frequency.

If any other point is chosen in the downstream of the channel, the flow exhibits the same periodicity nature as that at the point (10, 1, 4), but with small amplitude. As u, v, and w are the system's variables, the 3-D phase portrait is depicted by plotting u against v and w. Thus, the phase portrait is nothing but the projection of the attractor on the x-y-z plane. Figure 11 shows the time-series, phase portrait, and power spectrum at Re=740. The time-varying solutions, in Fig. 10(a), show the existence of maximum and minimum solutions for the u-velocity component. Hence the corresponding phase portrait in Fig. 10(b) exhibits a periodic attractor. Further from the power spectrum plotted in Fig. 10(c) a dominant frequency is noticed at f_1=9 and the other weak frequency at f_2=18. It can be observed that these two frequencies are arithmetically related to each other in the sense that f_2=$2f_1$. Hence, there occurs a frequency-doubling bifurcation. The presence of frequency-doubling bifurcation is a precursor to the onset of chaos in the nonlinear system. This frequency-doubling bifurcation occurred when the simulated stable limit cycle became unstable with the primary frequency f_1 and it is surrounded by the stable limit cycle of twice the frequency of f_1, i.e., f_2=$2f_1$. From Fig. 10(b), it is observed that a solution point on the limit cycle remained in the curve all the time and returned to the initial point periodically with a small deviation due to the presence of the subharmonic frequency, f_2. When Re was increased, the frequencies become higher although the bandwidths of individual frequencies have become narrow.

Figure 11 shows the time-series solution, 3-D phase portrait, and a power spectrum at Re=1000. The 3-D phase portrait, shown in Fig. 11(b) [corresponding to the time-series solution in Fig. 11(a)], changes its pattern from the phase portrait of Re=740 due to the presence of two more frequencies. The amplitude of the fundamental frequency has increased from 0.0425 to 0.0975. Also, the four frequencies, f_1=18, f_2=$2f_1$, f_3=$3f_1$, and f_4=$4f_1$, are arithmetically related to each other. Those additional peaks were subharmonic to the fundamental frequency f_1. These new spectral peaks were the "sidebands" about the primary frequency f_1 that came into existence through the frequency-doubling bifurcation of the frequency one orbit. Sidebands are the spectral peaks distributed symmetrically on both sides of the frequency peak at intervals equal to the integer multiples of the modulating frequency.[24,25]

When Re was further amplified to 1363, the 3-D phase portrait and the power spectrum (Fig. 12) show different trends. In the power spectrum, although the amplitude of the fundamental frequency is increased, as shown in Fig. 12(b), there exists an infinite number of arithmetically related frequencies with a small amplitude. More generally, the power spectrum of a frequency n orbit consists of a family of discrete peaks for the primary frequency and its overtones. In the periodic motion, all these peaks were rationally related to the primary peak (resonance).

The relationship between the frequency-doubling bifurcation and the KH instability can be explored as follows from Figs. 10–12. In Fig. 11(c) the frequency spectra of the u velocities at the points P1, P2, and P3 chosen at the channel midspan are shown. The locations of these points and the u-velocity contours are shown in Fig. 11(d). The fundamen-

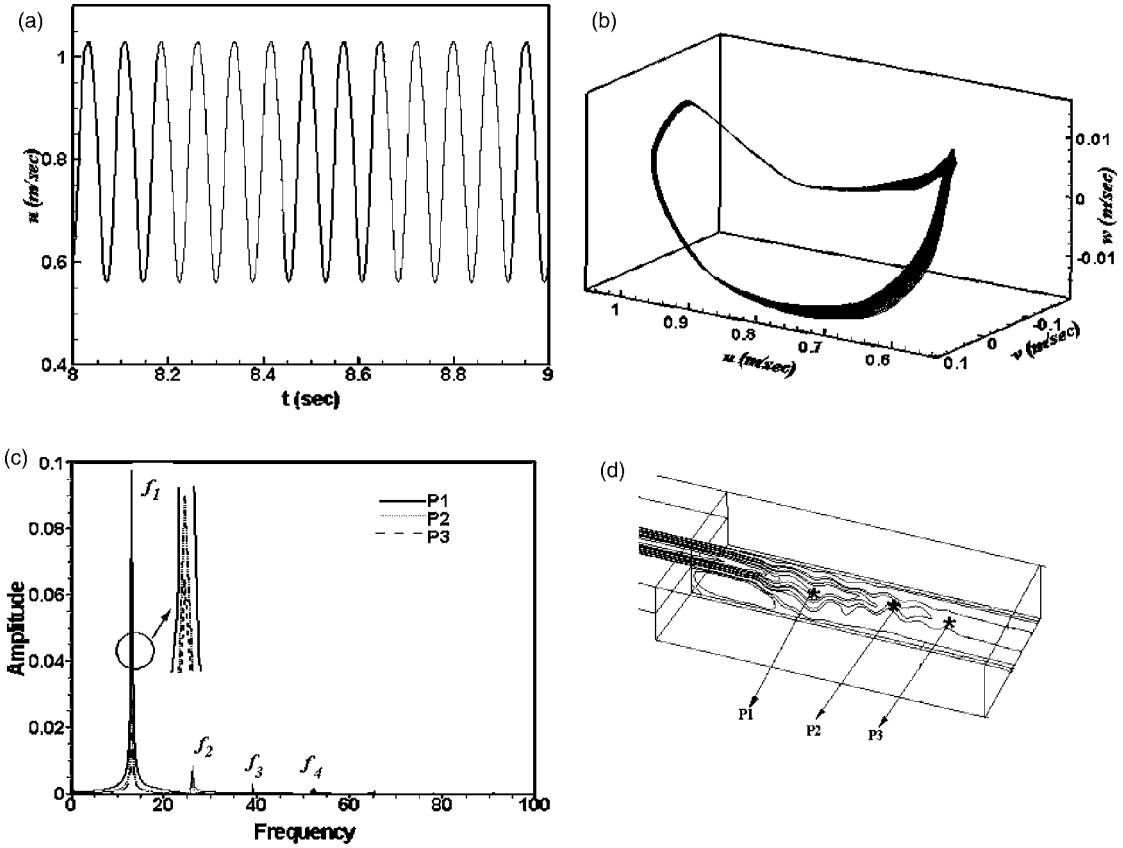

FIG. 11. The simulated (a) time-series; (b) phase portrait based on the solutions obtained at the point P1 (10, 1, 4) for Re=1000. The power spectrum for Re=1000 in (c) is based on the time-series solutions obtained at the points P1, P2, and P3. f_1(=18), f_2(=$2f_1$), f_3=($3f_1$), and f_4=($4f_1$) denote the fundamental frequency and the three arithmetically related frequencies. These four frequencies acknowledge the presence of the frequency-doubling bifurcation. The three arbitrary points P1 (10, 1, 4), P2 (15, 1, 4), and P3 (20, 1, 4) shown in (d) are chosen downstream of the centerline of the backward facing step channel. The dark (orange) to light (blue) contour lines represent the maximum to minimum u velocity, respectively.

tal frequency, f_1, in the spectrum corresponds to the inflow oscillation frequency and the most amplified mode of KH instability. Also, for all the investigated cases, the inflow oscillation of the fundamental frequency f_1 is identical to the most amplified mode of the KH instability. This direct triggering of the most unstable KH mode results in a rapid growth of the KH instability, which explains the stronger triggering of the KH instability as Re is amplified from 740 to 1363. The small amplitude frequencies are arithmetically related to each other and to the fundamental frequency. These frequencies result in a slower development of the KH instability, which is responsible for the roll-up of the shear layer.

In the above discussion, it is shown that the maximum streamwise extent of the separation region depends mostly on Re. The increasing Re strongly triggers the KH instability and promotes the decay of the recirculation region into small regions (as shown in Fig. 8). Hence triggering the most unstable KH instability by an appropriate choice of Re can significantly promote the decay of the recirculation region. Similar oscillation regimes were observed by Wissink[26] in the separating and transitional flow over a flat plate.

It was observed that the frequency-doubling bifurcation kept occurring, but with the shorter and shorter interval of increasing Re. Eventually, an infinite number of fundamental frequencies was observed and the path of the solution did not repeat any longer. At this moment chaos sets in. Figure 13 shows the onset of chaotic flow at Re=2000. The corresponding phase portrait, and power spectrum are shown in Figs. 13(i) and 13(ii), respectively. The phase portrait in Fig. 13(i) exhibits a chaotic attractor. The corresponding power spectrum in Fig. 13(ii) is marked with a rich spectral structure. Such a broadband power spectrum shows the existence of a continuum of frequencies. The corresponding frequencies cannot be predicted for this Re=2000. The simulated nonlinear resonances are directly related to the unstable periodic orbits embedded within the chaotic attractor. As a result, the power spectrum for the predicted chaotic attractor indeed can provide some information concerning the dynamics of the system, namely, the existence of unstable periodic orbits (nonlinear resonances) that can strongly influence the recurrence properties of the chaotic orbit. Hence, at Re =2000, the specific condition or system state at or near the attractor is entirely unpredictable.

In Fig. 14 the unsteady solutions are analyzed at two time intervals. One time interval is considered from t=8 to 9 s and the other from t=9 to 10 s of the flow at Re=2000. The time series before 9 s did not show the totally disorganized flow nature. The corresponding 3-D phase portrait in Fig. 14(b) showed a nonchaotic attractor and the power spectrum in Fig. 14(c) showed three visible arithmetically related frequencies. When the time was amplified fur-

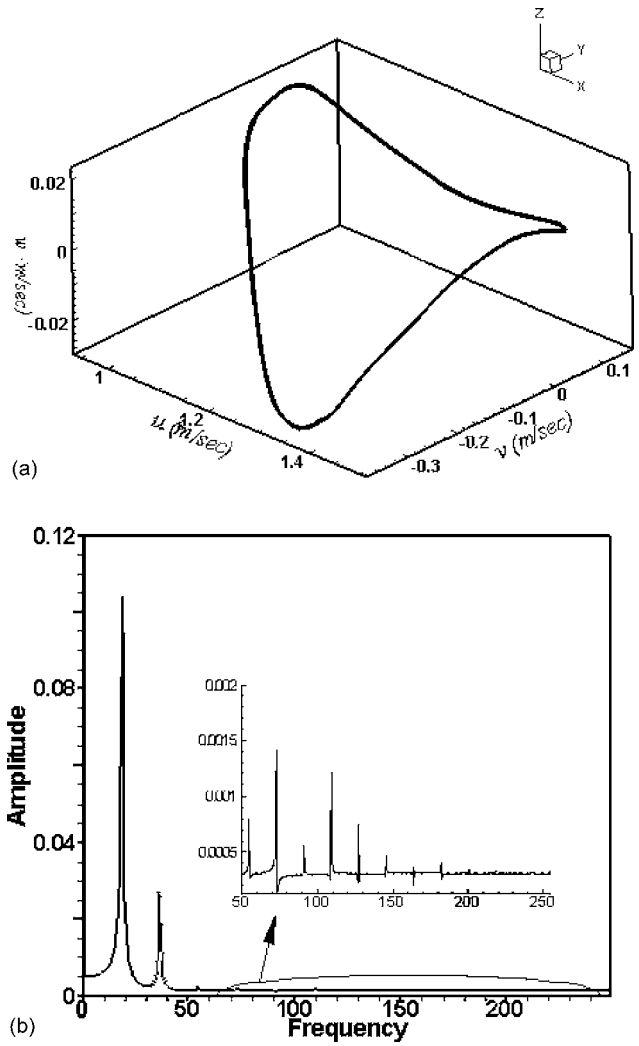

FIG. 12. The simulated (a) 3-D phase portrait and (b) power spectrum for Re=1363 based on the solutions obtained at the point (10, 1, 4).

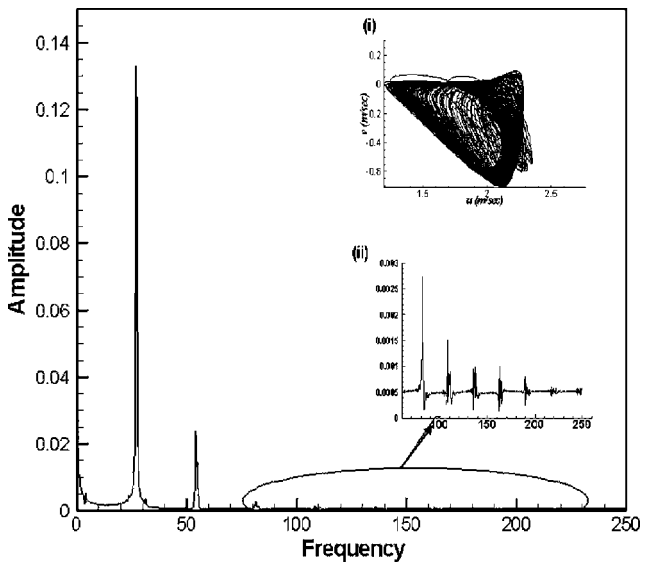

FIG. 13. For Re=2000, the (i) phase portrait; (ii) power spectrum based on the solutions obtained at the point (10, 1, 4).

ther, i.e., $t>9$, the disorganized solutions were observed and were shown in Fig. 14(d). The corresponding 3-D phase portrait in Fig. 14(e) illustrated a chaotic attractor and the power spectrum in Fig. 14(f) showed one principle frequency and an infinite number of subharmonic frequencies. Normally, these simulated chaotic attractors are generally found in the turbulence problems only. These attractors turn the complex system into turmoil. The configuration of attractors in phase space can help us to determine whether the investigated system is conservative or dissipative. The predicted attractors are also useful to understand more about the chaotic behavior of the system under current investigation. Ruelle[27] called the chaotic attractor of turbulence system as the strange attractor. He found that this attractor pulled complex systems into a space of fractional dimension.[28]

3. Pitchfork bifurcation

The presence of pitchfork bifurcation is observed at Re=2000 and is characterized by the appearance of a symmetry-breaking solution in the symmetric physical domain. In the literature, such a symmetry breaking flow phenomenon in the symmetric channels is termed as Coanda effect.[29] Usually, the pitchfork bifurcation is of the static and local type and involves one or more equilibrium solutions. In the nonlinear system with the geometric and flow symmetry, the perturbations of different sorts may initiate the pitchfork bifurcation. The currently investigated backward-facing step problem shows spanwise symmetry in both the geometry and boundary conditions. As the solution started to bifurcate, the geometrically symmetric fluid flow lost its symmetry and the stable branch became unstable. This led to the formation of two new stable branches. Hence this pitchfork bifurcation solution is called as the symmetry-breaking solution.

In Fig. 15 the streamwise velocity contours along various cross sections are compared at different time levels for Re=2000. Figure 15 clearly illustrates the evolution of the pitchfork bifurcation along x/S (=10) and y/S (=0.05, 1.9875) planes. It was observed that this bifurcation occurs in the spanwise direction as shown in Fig. 15. At t=6 s the flow showed the symmetric nature but when time proceeds the flow lost its symmetric nature with respect to the symmetry plane ($z/S=4$), as shown in Figs. 15(a)–15(c). Extensive numerical verification was made to ascertain that the simulated pitchfork bifurcation was not of numerical origin. Table I shows the u-velocity L_2 error norms, at different cutting planes during different time steps, between the two halves of the channel. It is noted that at the smaller time interval the L_2 error norm is smaller. The L_2 error norm increases with time, which gives the evidence for the existence of the pitchfork bifurcation. Similar symmetry breaking observation was reported by Nie and Armaly[1] in their experimental work for the transitional flow. Thus, it can be inferred that the chaotic motion starts with a Hopf bifurcation, proceeds with frequency-doubling bifurcation, and finally ends with a pitchfork bifurcation.

V. CONCLUDING REMARKS

Nonlinear dynamics in the recirculation region that is developed adjacent to the step wall of a three dimensional

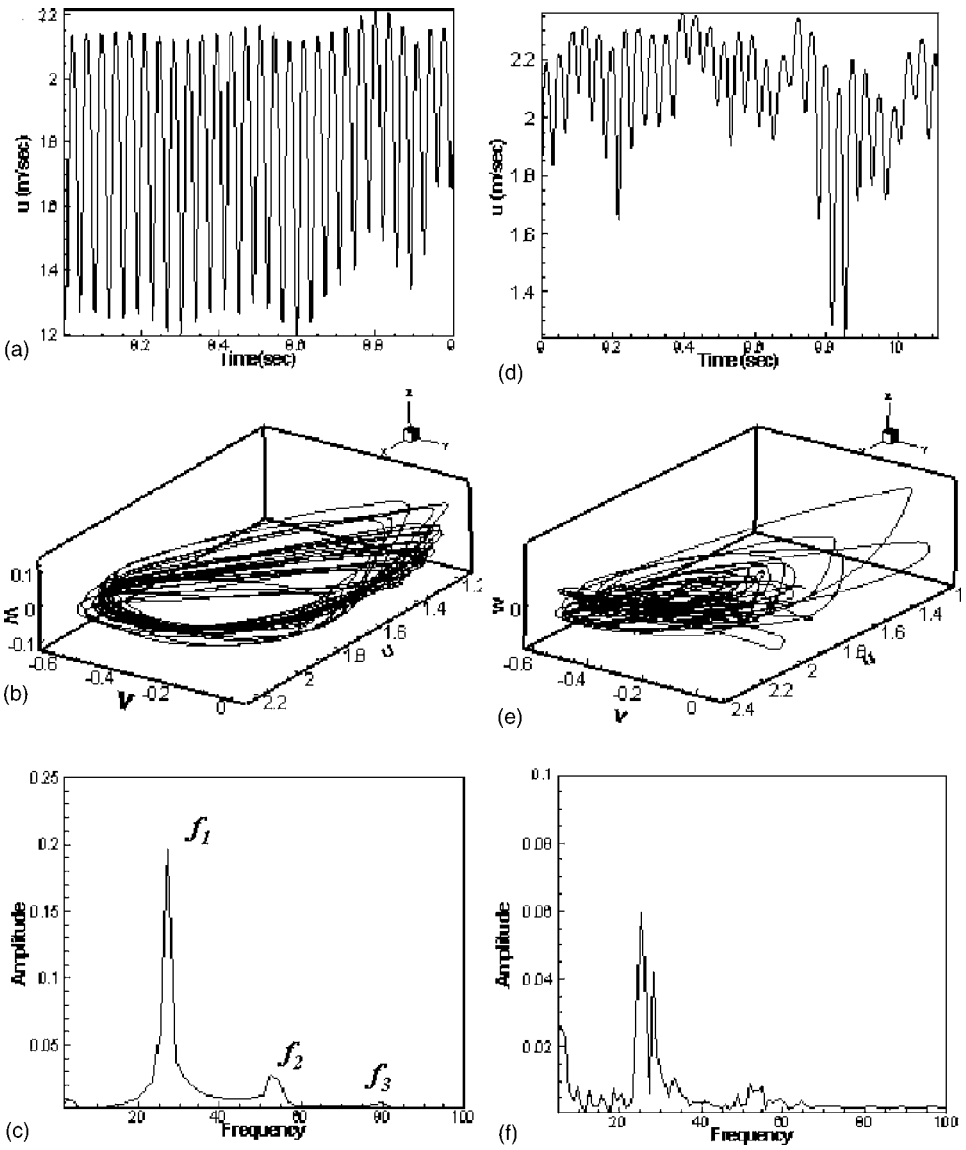

FIG. 14. The simulated (a), (d) time series, (b), (e) 3-D phase portrait, and (c), (f) power spectrum for the case considered at Re=2000. (a), (b), (c) are based on the simulated solutions from $t=8$ to 9 s and (d), (e), (f) are based on the simulated solutions from $t=9$ to 10 s.

backward-facing step flow is presented as a function of the control parameter, namely, the Reynolds number. The simulated results show the good agreement with the experimental results of Nie and Armaly[1] and Armaly and others.[4] The nonlinear theory was studied based on the vortex stability and bifurcation. The transitional flow leading to the chaotic flow is analyzed based on the limit cycles, time series, phase portraits, power spectrums, and L_2 error norms for a wide range of Reynolds numbers. The flow simulation results of the present study can be summarized as follows:

- The maximum streamwise extent of the recirculation region depends on time and Re, which in turn determines the duration of the deceleration period and the strength of the deceleration, respectively. The apparently triggered Kelvin-Helmholtz (KH) instability leads to a faster roll-up of the shear layer, illustrated by the fact that the maximum reverse flow was reached at an earlier phase to promote the subsequent damage of the larger separation region, near the step wall, as it was convected downstream.
- The flow path in the current nonlinear system consists of one large limit cycle surrounded by two small similar limit cycles. These limit cycles divide the vortex into the inner unstable region and the outer stable region. Hence, the present channel flow was trapped by the stable limit cycles and made to proceed with the sustained oscillation, which confirms the existence of a supercritical Hopf bifurcation.
- Increasing Re strongly triggers the KH instability and promotes the decay of the recirculation region. The higher amplitude of the fundamental frequency corresponds to the rapid growth of the KH instability while the smaller frequency amplitudes correspond to the roll-up of the shear layer.
- The frequency and amplitude of oscillations changed with the increasing values of Re. The oscillation started with one dominant fundamental frequency and its subharmonic frequencies. All frequencies are arithmetically related to each other, thus confirming the existence of the frequency-doubling bifurcation.
- For Re=2000, the time series solutions showed the slow development of an aperiodic flow. A fast Fourier

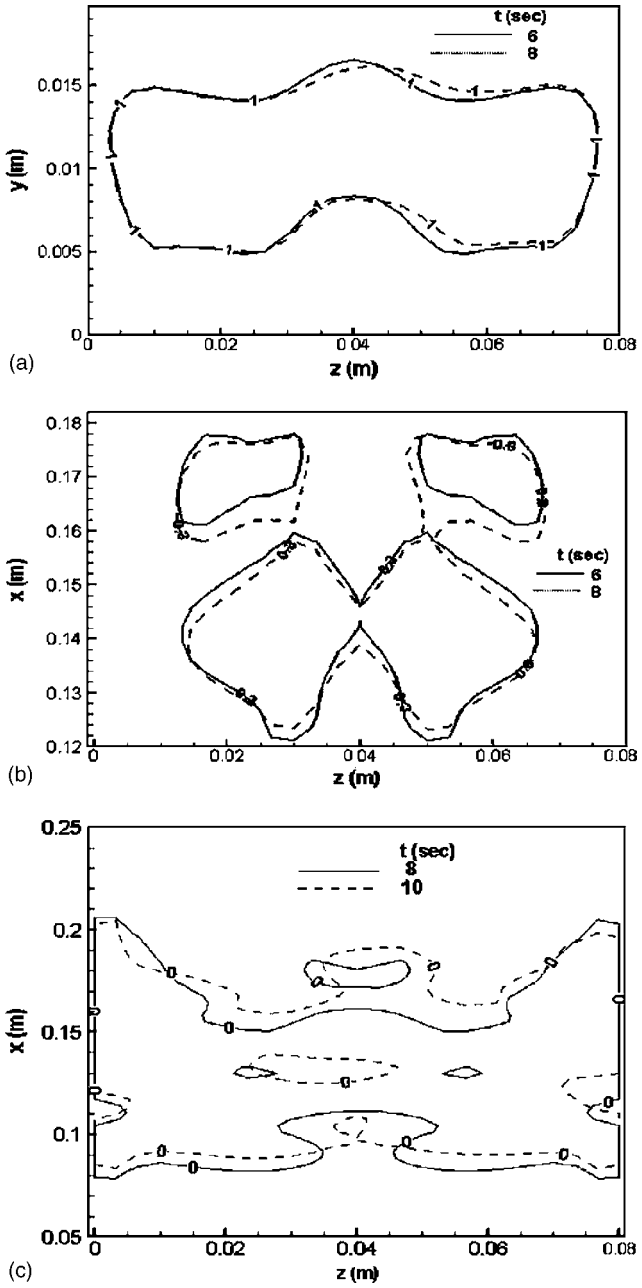

FIG. 15. The simulated streamwise velocity contours along various cross sections with contour levels in numbers at (a) $x=0.1$ m, (b) floor ($y=0.0005$ m), and (c) roof ($y=0.019\,75$ m) plane to show the existence of pitchfork bifurcation for Re=2000 at various times. Solid and dotted lines denote the symmetric and asymmetric contours, respectively.

analysis of the simulated time-series velocity component at the arbitrarily chosen point exhibited a single fundamental frequency to an infinite number of frequencies. Also in the power spectrum, a simple attractor evolves to chaotic attractor as the time proceeds. Moreover, the initial symmetric solution became unsymmetric leading to the pitchfork bifurcation.

TABLE I. The simulated u velocity L_2 error norms at Re=2000.

Plane	$t=6$ s	$t=8$ s
$x/S=10$	$0.632\,93\times10^{-5}$	$0.748\,686\times10^{-3}$
$y/S=0.05$ (floor)	$0.984\,213\times10^{-5}$	$0.384\,08\times10^{-3}$
$y/S=1.975$ (roof)	$0.332\,722\times10^{-7}$	$0.764\,748\times10^{-3}$

ACKNOWLEDGMENT

The financial support from National Science Council, under NSC 94-7611-E-002-021 of THE Republic of China, is gratefully acknowledged.

[1] J. H. Nie and B. F. Armaly, "Reverse flow regions in three-dimensional backward-facing step flow," Int. J. Heat Mass Transfer **47**, 4713 (2004).
[2] R. J. Goldstein, V. L. Eriksen, R. M. Olson, and E. R. G. Eckert, "Laminar separation, reattachment, and transition of the flow over a downstream-facing step. Trans. ASME D," J. Basic Eng. **92**, 732 (1970).
[3] M. K. Denham and M. A. Patrick, "Laminar flow over a downstream-facing step in a two dimensional flow channel," Trans. Inst. Chem. Eng. **52**, 361 (1974).
[4] B. F. Armaly, F. Durst, J. C. F. Pereira, and B. Schónung, "Experimental and theoretical investigation of backward-facing step flow," J. Fluid Mech. **127**, 473 (1983).
[5] E. W. Adams and J. P. Johnston, "Effects of the separating shear-layer on the reattachment flow structure. Part 2: Reattachment length and wall shear-stress," Exp. Fluids **6**, 493 (1988).
[6] B. J. Bayly, S. A. Orszag, and T. Herbert, "Instability mechanisms in shear-flow transition," Annu. Rev. Fluid Mech. **20**, 359 (1988).
[7] K. M. Butler and B. F. Farrell, "Optimal perturbations and streak spacing in wall-bounded turbulent shear-flow," Phys. Fluids A **5**, 774 (1993).
[8] J. M. Hamilton, J. Kim, and F. Waleffe, "Regeneration mechanisms of near-wall turbulence structures," J. Fluid Mech. **287**, 317 (1995).
[9] R. K. Avva, "Computation of the turbulent flow over a backward-facing step using the zonal modeling approach," Ph.D. thesis, Stanford University, 1988.
[10] L. Kaiktsis, G. E. Karniadakis, and S. A. Orszag, "Onset of three-dimensionality, equilibrium and early transition in flow over a backward-facing step," J. Fluid Mech. **231**, 501 (1991).
[11] L. Kaiktsis, G. E. Karniadakis, and S. A. Orszag, "Unsteadiness and convective instabilities in two-dimensional flow over a backward-facing step," J. Fluid Mech. **321**, 157 (1996).
[12] K. Akselvoll and P. Moin, "Large eddy simulation of a backward-facing step flow," in *Engineering Turbulence Modeling and Experiments* (Elsevier, Amsterdam, 1993).
[13] H. Le, P. Moin, and J. Kim, "Direct numerical simulation of turbulent flow over a backward-facing step," J. Fluid Mech. **330**, 349 (1997).
[14] K. N. Ghia, G. A. Osswald, and U. Ghia, "Analysis of incompressible massively separated viscous flows using unsteady Navier-Stokes equations," Int. J. Numer. Methods Fluids **9**, 1025 (1989).
[15] D. K. Gartling, "A test problem for outflow boundary conditions—flow over a backward-facing step," Int. J. Numer. Methods Fluids **11**, 953 (1990).
[16] P. M. Gresho, D. K. Gartling, J. R. Torczynski, K. A. Cliffe, K. H. Winters, T. J. Garratt, A. Spence, and J. W. Goodrich, "Is the steady viscous incompressible two-dimensional flow over a backward-facing step at Re=800 stable?" Int. J. Numer. Methods Fluids **17**, 501 (1993).
[17] A. Fortin, M. Jardak, J. J. Gervais, and R. Pierre, "Localization of Hopf bifurcations in fluid flow problems," Int. J. Numer. Methods Fluids **24**, 1185 (1997).
[18] P. T. Williams and A. J. Baker, "Numerical simulations of laminar flow over a three-dimensional backward-facing step," Int. J. Numer. Methods Fluids **24**, 1159 (1997).
[19] B. F. Armaly, A. Li, and J. H. Nie, "Measurements in three-dimensional laminar separated flow," Int. J. Heat Mass Transfer **46**, 3573 (2003).
[20] H. Hakin, *Instability Hierarchies of Self Organizing Systems and Devices in Advanced Synergetics* (Springer-Verlag, Berlin, 1984).
[21] P. Grassberger and I. Procaccia, "Characterization of strange attractors," Phys. Rev. Lett. **50**, 346 (1983).
[22] G. E. Lixin and C. A. I. Qingdong, "The topology of the sectional streamlines," Commun. Nonlinear Sci. Numer. Simul. **3**, 203 (1998).
[23] M. Kiya and K. Sasaki, "Structure of large-scale vortices and unsteady reverse flow in the reattaching zone of a turbulent separation bubble," J. Fluid Mech. **154**, 463 (1985).

[24] A. Hund, *Frequency Modulation* (McGraw-Hill, New York, 1942).
[25] J. A. Rial and C. A. Anaclerio, "Understanding nonlinear responses of the climate system to orbital forcing," Quaternary Science Reviews **19**, 1709 (2000).
[26] J. G. Wissink, "Separating, transitional flow affected by various inflow oscillation regimes," ANZIAM J. **46**, C117 (2005).
[27] David Ruelle, *Chaotic Evolution and Strange Attractors* (Cambridge University Press, Cambridge, England, 1989).
[28] J. Briggs and F. D. Peat, *The Turbulent Mirror: An Illustrated Guide to Chaos Theory and the Science of Wholeness* (Harper and Row, New York, 1989).
[29] R. Wille and H. Fernholz, "Report on the first European Mechanics Colloquium on the Coanda effect," J. Fluid Mech. **23**, 801 (1965).